Neutralization and wake effects on the Coulomb explosion of swift H_2^+ ions traversing thin films

L. F. S. Rosa, P. L. Grande, J. F. Dias, and R. C. Fadanelli

Ion Implantation Laboratory, Institute of Physics, Federal University of Rio Grande do Sul, Av. Bento Goncalves,
9500, CP 15051, CEP 91501-970, Porto Alegre, RS, Brazil

M. Vos

Atomic and Molecular Physics Laboratories, Research School of Physics and Engineering,
The Australian National University, Canberra 0200, Australia

The Coulomb explosion of small cluster beams can be used to measure the dwell time of fragments traversing amorphous films. Therefore, the thickness of thin films can be obtained with the so-called Coulomb depth profiling technique using relatively high cluster energies where the fragments are fully ionized after breakup. Here we demonstrate the applicability of Coulomb depth profiling technique at lower cluster energies where neutralization and wake effects come into play. To that end, we investigated 50–200 keV/u H_2^+ molecular ions impinging on a 10 nm TiO_2 film and measured the energy of the backscattered H^+ fragments with high-energy resolution. The effect of the neutralization of the H^+ fragments along the incoming trajectory before the backscattering collision is clearly observed at lower energies through the decrease of the energy broadening due to the Coulomb explosion. The reduced values of the Coulomb explosion combined with full Monte Carlo simulations provide compatible results with those obtained at higher cluster energies where neutralization is less important. The results are corroborated by electron microscopy measurements.

PACS number(s): 34.50.Bw, 34.80.Bm, 34.50.Fa

I. INTRODUCTION

The determination of the thickness of thin films is an important task in many areas of modern technology and can be accomplished with a variety of techniques including those that make use of ion and electron beams. For most of them, a knowledge of the atomic density is required. Recently [1], a novel technique based on the Coulomb explosion of H_2^+ molecular beams [2–4] has been developed. The so-called Coulomb depth profiling technique is based on the fact that once H_2^+ ions of few hundred keV penetrate the first monolayers of a solid, they lose their bound electrons and break up under the Coulomb repulsion force between the fragments. Consequently, the internuclear distance r and the relative speed between the fragments increase, leading to different energies in the laboratory frame and giving rise to a peculiar energy-loss straggling referred to as Coulomb broadening σ_C [1]. In addition, a fragment can be backscattered at a depth z and detected when it leaves the sample. For energies higher than typically a few keV/nucleon, most ion trajectories are V shaped and effects due to correlated motion of the fragments take place only along the incoming path before the backscattering collision. The Coulomb broadening σ_C can be then obtained by measuring the energy loss of these fragments in comparison with the reference energy loss taken with H^+ ions at the same energy per nucleon. The depth information is obtained from the broadening of the energy-loss distribution of backscattered H^+ ions formed after the breakup of the H_2^+ clusters. The energy-loss straggling can be disentangled from other energy-loss fluctuations and converted to dwell time or penetration depth [1]. This technique thus provides film thicknesses in nm. Therefore, by combining the thickness as measured by the Coulomb explosion (in nm) with the thickness measured by traditional ion scattering (in $\mu g/cm^2$) one can obtain the density.

However, the conversion of the energy-loss straggling due to the Coulomb explosion to dwell time is not straightforward for H_2^+ clusters with energies lower than 100 keV/u, where neutralization, multiple-scattering and wake-potential effects cannot be neglected. For this case, Monte Carlo simulation is the appropriate tool to investigate the influence of such effects on the Coulomb explosion of H_2^+ clusters.

For low energies, the neutralization of fragments during the Coulomb explosion has been discussed in the literature in connection with the existence of H^0 inside the solid. Brandt and the Lyon group [5] have claimed that the neutral fraction is composed basically of H^+ ions that are neutralized when the outgoing trajectory crosses the surface. On the contrary, Cross [6] has argued in favor of the neutral fraction inside the solid whose value can be understood in terms of electron capture into, and subsequent loss from, bound states of the moving proton. Most of the subsequent work (see, for example, Ref. [7]) assumes that the fraction of H^0 stems from inside the solid, but the question whether there is a stable H^0 fraction inside the solid with an electron as tightly bound and localized as in vacuum still remains.

The role of the wake potential during the Coulomb explosion has been much less investigated since only recently methods to describe the interaction between the valence electrons of a solid and the cluster beam using reliable dielectric functions have been developed for different materials [8–11]. In fact, the wake potential can affect the Coulomb explosion in different ways. Its symmetrical part screens the Coulomb interaction between the H^+ fragments. Moreover, it decreases the electron binding energy for the embedded neutral fragments, leading to an increase of their atomic radii. In addition, the asymmetrical part of the wake potential can even increase the Coulomb explosion as will be shown later.

Apart from a few exceptions [12,13], most of the previous investigations of the Coulomb explosion in solids have used the

Yukawa potential to model the screening interaction between the fragments. Moreover, the effect of the full noncentral wake potential on the explosion involving fragments that are charged part of the time has not been fully explored. This issue plays a key role on the conversion of Coulomb explosion to dwell time at low as well as at very high cluster energies.

Understanding of the Coulomb explosion at lower energies is interesting in itself, but also has practical value, as at lower cluster energies the technique can be applied to thinner layers. The aim of the present work is to demonstrate that the Coulomb profiling technique yields good results at relatively low cluster energies, provided neutralization and wake effects are taken into account properly. Therefore, unlike Ref. [1] where it was assumed that fully ionized fragments interact with a Yukawa potential, the present work investigates how valence electrons from a solid affect the Coulomb explosion of embedded fragments. To that end we have investigated many effects such as the presence of dressed H^0 projectiles with modified atomic radius, vicinage effects on projectile charge states and noncentral interaction effects. Experimentally thin TiO_2 layers grown on Si were analyzed with the medium energy ion scattering (MEIS) technique [14], which is a refinement of the traditional Rutherford backscattering spectrometry (RBS) [15]. This is the best technique to determine the Coulomb broadening for films thinner than 10 nm [1] because of its excellent energy resolution. Unless otherwise stated, atomic units ($n = m_e = e = 1$) are used throughout the paper.

II. EXPERIMENTAL PROCEDURE AND DATA ANALYSIS

The MEIS technique was used in the present work in order to demonstrate the applicability of the Coulomb depth profiling technique for the measurement of thin films employing 50–200 keV/u H_2^+ molecular ions. The sample consisted of a thin TiO_2 film grown on the native silicon oxide present on the surface of a (100) Si wafer and was mounted on a 3-axis goniometer inside the scattering chamber with a vacuum of about 10^{-7} mbar. Typical beam currents were less than 15 nA. The ion source provides H_2^+ molecules without any preferential orientation.

Different angles of incidence were used in order to increase the apparent thicknesses of the films. The backscattered H^+ ions emerging from the target were analyzed using a toroidal electrostatic analyzer (TEA) mounted at 120 degrees with respect to the beam direction. At the top end of the TEA a set of two microchannel plates coupled to a position-sensitive detector allows each ion to be energy- and angle-resolved, leading to two-dimensional (2D) spectra. The TEA angular aperture is 24°, covering angles from 108° to 132°. Each angle bin corresponds to 0.08 degrees. The overall energy resolution of the system is 300 eV for a 100 keV H^+ beam.

A typical 2D MEIS spectrum obtained for 175 keV/u H_2^+ projectiles striking the TiO_2 film is depicted in Fig. 1. The contributions from protons backscattering from Ti, Si, and O are easily distinguished in this figure. Moreover, the contribution from a thin C layer (due to contamination) can be seen in the 2D spectrum as well as the effect of blocking on the Si intensity along the (100) direction. For elements at the surface of the sample (Ti, O, and C), the signals have different
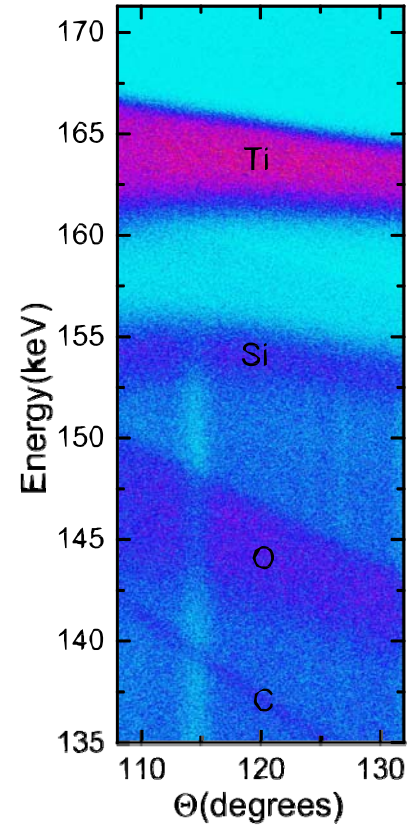

FIG. 1. (Color online) 2D MEIS spectrum measured with 175 keV/u of H_2^+ projectiles under normal incidence on the TiO_2 layer grown over crystal Si. The following signals are observed from top to bottom: Ti from the TiO_2 film; Si from the substrate; O from TiO_2 and SiO_2 films; and C stemming from contamination. Blocking lines in Si are also visible. See text for further information.

slopes according to the dependence of the kinematic factor on the scattering angle.

The 1D energy spectrum featuring the Ti signal for a scattering angle of 120° is shown in Fig. 2. The 1D spectrum is obtained through the projection of the 2D spectrum on the energy axis for a particular set of angle bins. In order to improve the counting statistics, several angle bins are integrated. In this case (for Ti part of the spectrum) corrections stemming from the dependence of the kinematical factor on the scattering angle, and from the depth of the backscattering events are properly taken into account.

The dashed line shown in Fig. 2 corresponds to the simulations of the energy spectrum generated by the POWERMEIS code for atomic ions [16], which essentially simulates the energy-loss spectrum according to the backscattering yield $Y(E)$ modeled as

$$Y(E) = A \int_0^t dz \, G\left(K E_0 - E - zS, \ \overline{\sigma_0^2 + zW^2} \right), \quad (1)$$

for a uniform film of thickness t. E_0 is the beam energy, K is the kinematic factor [17], and $G(E,\sigma)$ is the Gaussian function with standard deviation σ. Moreover, S and W^2 are the stopping power and straggling factors respectively as defined in Ref. [17], while σ_0 is the overall energy resolution of
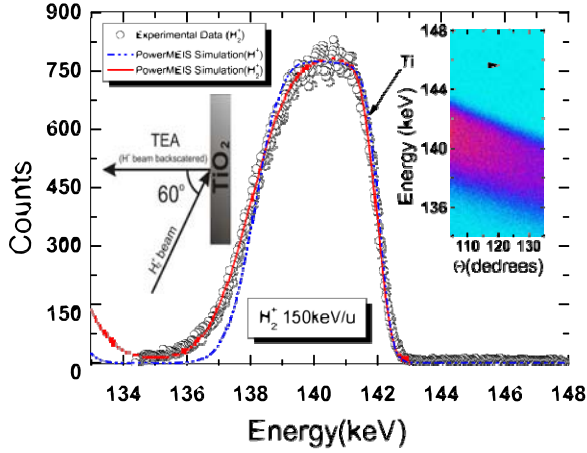
FIG. 2. (Color online) 1D energy spectrum obtained by 150 keV∕nucleon H_2^+ molecules striking on TiO_2. The inset shows the 2D spectrum featuring the Ti signal obtained with the H^+ beam. The best fittings to the H_2^+ data (red line) and to the H^+ data (blue line) obtained for the Ti signal were obtained through simulations using the POWERMEIS code. Note that the H^+ data were omitted from the picture for the sake of clarity.

TABLE I. Values used in the POWERMEIS code [16] to simulate the MEIS spectra.

Energy (keV/u)	Stopping (eV/Å)	Straggling (eV²/Å)	$\sigma_0(H^+)$ (eV)	$\sigma_0(H_2^+)$ (eV)
50	16.4	870	210	240
60	17.3	1000	245	485
80	18.0	1200	330	375
100	18.1	1250	400	460
120	17.8	1500	480	530
150	17.0	1750	600	670
175	16.2	2000	700	760
200	15.4	2100	800	900

the detection system and A is an overall constant that depends on the elastic cross section, solid angle, and ion fluence.

In case of molecular ions (solid line in Fig. 2), the Gaussian function mentioned above has to be convoluted with the energy distribution due to the Coulomb explosion modeled as [1]

$$F_{mol}(\Delta E, z) = \frac{1}{2\sqrt{3}\sigma_c(z)} \mathcal{S}(\Delta E + \sqrt{3}\sigma_c(z))$$
$$\times \mathcal{S}(\sqrt{3}\sigma_c(z) - \Delta E). \quad (2)$$

Here ΔE is the energy change (in the laboratory frame) of an ion due to the coulomb explosion, $\mathcal{S}(\Delta E)$ is the Heaviside function and $\sigma_c(z)$ is the contribution of the Coulomb explosion to the energy-loss straggling at a distance z inside the solid after the molecular breakup. $F_{mol}(\Delta E, z)$ takes into account all possible angular orientations after the breakup. Here, the Coulomb explosion is parametrized according to Ref. [1] as $\sigma_c(z) = \gamma z$, where γ is a free parameter to be determined from a best fit to the experimental data. The Coulomb broadening σ_C is the value of $\sigma_c(z)$ taken when z corresponds to the the film thickness. All other parameters are the same for H^+ and H_2^+ projectiles with the exception of the σ_0, which is slightly larger in case of molecular projectiles because of the intrinsic momentum distribution of a proton that is part of a molecule (Doppler effect) before the molecular breakup.

The stopping power used in the simulations are those given by the SRIM2010 code [18] and corrected by recent measurements from Ref. [19], while the initial energy-loss straggling values are given by the straggling theory developed by Lindhard and Scharff [20]. The energy-loss straggling values were relaxed during the fitting procedure through the minimization of the reduced χ^2 (see values in Table I). Once the amount of TiO_2 in the overlayer (in terms of atoms/cm²) and energy-loss straggling parameters were determined for the proton case, they were kept constant throughout the analysis concerning H_2^+ molecules.

The vicinage effect of the energy loss [21] is included in the analysis by considering a slight modification of the stopping power along the incoming path, i.e., before the backscattering event. For ultrathin films, the correction factor on the stopping power does not depend on the depth and is less than 15%. In addition, the energy loss at the backscattering collision is modeled using an asymmetrical line shape [22] with an asymmetry parameter of about 1∕200 eV^{-1} for Ti. Finally, effects arising from the intrinsic momentum distribution of protons that are part of the molecule mentioned above were included as a Gaussian distribution. Thus, these effects can be combined to the energy resolution, which amounts about 750 eV for 150 keV∕nucleon H_2^+ molecules.

According to Fig. 3 the MEIS energy spectrum taken with 150 keV∕u H_2^+ ions depends on the TiO_2 film density and thickness even for a fixed amount of atoms/cm² (here 1.54×10^{17} atoms/cm²). As it is well known, for H^+ projectiles the energy spectrum does not change with the atomic densities and thickness of the film as long as the number of atoms/cm² is constant. However, the Coulomb explosion is sensitive to the dwell time or absolute thickness of the film. Therefore, the use
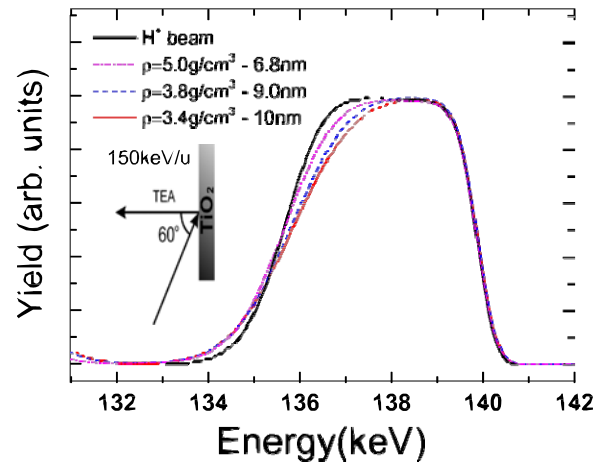

FIG. 3. (Color online) Simulated energy spectra for 150 keV∕nucleon H_2^+ molecules striking on TiO_2 with different atomic densities and thicknesses but with a fixed number of atoms/cm² (see text). The geometry is depicted in the inset. For comparison, the energy spectrum for protons with the same speed is shown by a black solid line.

of cluster ions allows for the identification of the film density or thickness separately.

Finally, transmission electron microscopy (TEM) measurements were performed in the cross-sectional samples prepared by ion milling. The samples were characterized by a JEM 2010 microscope in phase-contrast mode and by a Titan FEI microscope in STEM mode.

III. THEORETICAL PROCEDURE

In order to use the Coulomb depth profiling technique for the accurate measurement of film thicknesses, it is important to investigate the effects of neutralization, wake potential, and multiple scattering on the Coulomb explosion. To that end, a Monte Carlo simulation code was developed according to Ref. [7]. It is assumed that the H_2^+ molecule dissociates at the first TiO_2 layer and each fragment is followed by solving the classical equations of motion considering the interaction between the fragments (H^+ or H^0) and the target atoms (Ti or O atoms) and between the fragments themselves. The initial distribution of internuclear distances r_0 was taken from the work of Kanter et $al.$ [23] and the direction of explosion was taken to be random for each impinging molecular ion. Since the conventional projectile energy loss and the Coulomb explosion are nearly statistically independent, the electronic energy loss and the corresponding energy-loss straggling were set to zero in order to calculate only the Coulomb broadening values. In this way, the broadening values are directly obtained from the variance of the energies after the fragments traversed a given thickness.

For the interaction of the fragments with the target atoms, the Molière interatomic potential [24] is used, while for the interaction between the fragments we make use of the electrostatic potential (the Coulomb potential in case of the H^+-H^+ interaction) that is screened by the valence electrons of TiO_2. This screening is usually modeled in a more simplified way as a Yukawa-type potential with screening length given by v/ω_p, where v is the ion speed and ω_p is the plasmon energy of the medium. For the molecular beam, we use the dynamical screening determined from the wake potential in order to improve the description of the polarization forces acting upon each fragment.

A. TiO₂ wake potential

Once the charged fragments penetrate the solid, the medium reacts to the presence of the external charge and becomes dynamically polarized, giving rise to a wake potential formed behind each fragment. This induced potential is responsible for the stopping power of each projectile and modifies the interaction between the molecular fragments. Therefore, each positive charge attracts electrons from the medium as it passes through, generating a wake (of fluctuation) in the electron density mainly behind the leading particle. The interaction of the trailing particle with the electronic medium will be affected by the wake potential generated by the leading particle.

Assuming a linear response of the medium, the induced potential V_{ind} at the cylindrical coordinates z (z axis along

as

$$V_{\text{ind}}(\tilde{z},\rho) = \frac{Z_p}{2\pi^2} \int_0^\infty \frac{dk}{k} \int_0^{kv} d\omega J_0(\sqrt{k^2 - \omega^2/v^2})$$

$$\times \left\{ \cos\left(\frac{\omega\tilde{z}}{v}\right) \text{Re}\left[\frac{1}{E(k,\omega)} - 1\right] \right.$$

$$\left. - \sin\left(\frac{\omega\tilde{z}}{v}\right) \text{Im}\left[\frac{1}{E(k,\omega)} - 1\right] \right\}, \quad (3)$$

where $E(k,\omega)$ is the dielectric constant of the medium and $\tilde{z} = z - vt$ is the distance from the moving fragment. $J_0(x)$ is the zero-order Bessel function. As was done in Ref. [27] for HfO_2, the dielectric function was described by a set of Mermin dielectric functions [28]:

$$\text{Im}\left[\frac{1}{E(k,\omega)}\right] = \sum_i A_i \text{Im}\left[\frac{1}{E(k,\omega; \omega_i,\gamma_i)}\right]_{\text{Mermin}}, \quad (4)$$

where the coefficients A_i, ω_i, and γ_i for TiO_2 are given by Fuentes et $al.$ [29] according to the procedure used in Refs. [19,30] and are related to the intensity, position and damping of each oscillator representing each peak in the reflection electron energy loss spectroscopy (REELS) spectrum of TiO_2 extrapolated to the optical limit, $k = 0$. Nevertheless such a procedure may not exactly reproduce the original REELS data by Fuentes et $al.$ [29] because these experiments probe the dielectric function away from the optical limit.

In order to get a better description of the dielectric function, we have also measured the REELS spectrum using high-energy electrons (40 keV) impinging on the same target (TiO_2), which probes the dielectric function much closer to the optical limit. The REELS data are converted to the corresponding dielectric function according to the quantitative analysis of electron energy loss spectra (QUEELS) software package [31]. Thus, we used a sum of Drude-Lorentz oscillators to fit the experimental REELS spectrum using the QUEELS software package.

$$\text{Im}\left[\frac{-1}{E(k,\omega)}\right] = \sum_i \frac{A_i \gamma_i \omega}{\left[\omega_i^2(k) - \omega^2\right]^2 + (\gamma_i\omega)^2} \quad (5)$$

with the dispersion given by

incoming beam direction) and ρ can be calculated [25,26]

$$\omega_l(k) = \omega_l + \alpha \frac{\hbar k^2}{2m'} \qquad (6)$$

where α is usually taken to be near 1.0 for metals and close to 0 for insulators.

Extracting the dielectric function from a REELS measurement is complicated due to the contribution of surface plasmons. To minimize this problem, we used a high incoming energy of 40 keV. At such high energy, the recoil energy transferred by the electron to the scattering nucleus cannot be neglected, and this recoil energy is larger for electrons scattered from O compared to Ti (see Fig. 4, top panel). This causes an ambiguity in the energy loss due to electronic excitations. The part of the spectrum due to electrons scattered from O was removed using a deconvolution procedure described elsewhere [32]. From the resulting spectrum a normalized loss distribution was derived, as described in Ref. [33], which was fitted with a dielectric function using the QUEELS package. Under these high-energy conditions the shape of
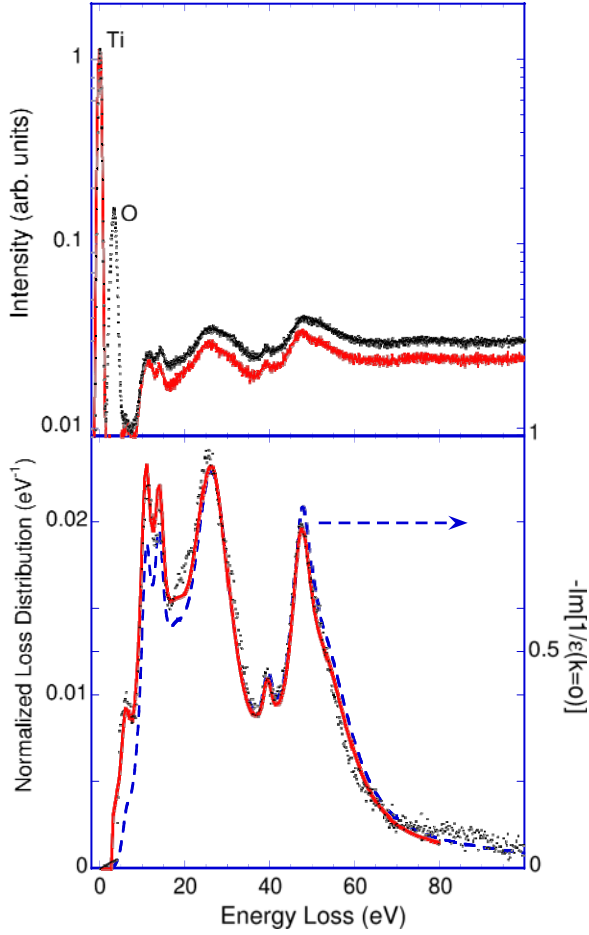
FIG. 4. (Color online) The top panel shows the measured REELS spectrum (dots) which shows separate elastic peaks for electrons scattered from Ti an O. After deconvolution of the O contribution (solid line) the spectrum can be treated in the same way as a low energy REELS spectrum. The bottom panel shows the obtained normalised loss function (dots), and a fit using a Drude-Lorentz dielectric function (solid line). The dashed line corresponds to the limit of $Im[−1/E(k,\omega)]$ for $k = 0$.

the normalized loss distribution is very close to the shape of $Im[−1/E(k,\omega)]$ for $k = 0$ as is illustrated in Fig. 4, bottom panel. The coefficients of the obtained fit are reproduced in Table II.

TABLE II. Drude-Lindhard parameters used in Eq. (5) for the fit in Fig. 4. α was taken to be 0.05.

ω_i (eV)	A_i (eV^2)	γ_i (eV)
6.2	1.65	2.4
11	16.8	3
14	17.9	3
18	25.5	7
27	266.9	12
39.5	16.6	3
47.5	124	5.5
53.5	366	17
90	102	50

For optical limit $k = 0$, the Drude-Lorentz and Mermin dielectric functions coincide for a given set of ω_i, A_i, and γ_i. However, since Eq. (3) involves an integration over the transfer momentum k, the values for the induced potential will differ for a Drude-Lorentz and Mermin dielectric functions, even if they coincide at $k = 0$. It should be pointed out that although we used $\alpha = 0.05$ as Fuentes *et al.* [29] to extract the dielectric function for TiO$_2$ from REELS measurements, we used $\alpha = 1$ to calculate the wake potential from Eq. (3) in order to improve the description of high-energy transfers.

In fact electron scattering measurements mainly probe electronic excitations with low momentum transfer. Ion stopping (as wake potential) is also sensitive to excitations at high momentum transfer [34]. Therefore, calculations of the ion stopping based on these REELS-derived dielectric functions fail when a small value of α is used. This is mainly due to the fact that the Bethe ridge part of the electronic excitations (binary collisions between particle and target electron, at high momentum transfer, where this particle acts as a free particle) implies that α is 1 at high momentum transfer. If we use the same oscillators as derived from a REELS experiment, but assuming a Mermin-type momentum dependence or an α value of 1, then we do get values for the ion stopping in reasonable agreement with experiment. Assuming a Mermin-type dispersion or $\alpha = 1$ would decrease the accuracy with which the REELS data are described. As a matter of fact, extracting the dielectric function with the right momentum dependence that is consistent with all sum rules is currently still an open question [35].

Figure 5 shows the wake potential from Eq. (3) for $\rho = 0$ as a function of $\tilde{z} = z − vt$ for a 150 keV H$^+$ ion in TiO$_2$ calculated with different dielectric functions. An inspection of Fig. 5 reveals that all wake potentials display an accumulation of negative charge, i.e., excess valence electron density behind the projectile. In spite of the differences between the use of Mermin-type and Drude-type dielectric functions and corresponding induced potentials, they yield very similar electronic stopping power values (proportional
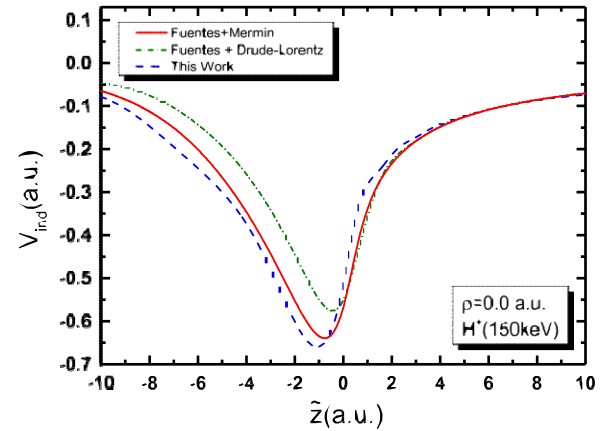

FIG. 5. (Color online) Wake potential at $\rho = 0$ as a function of $\tilde{z} = z − vt$ for 150 keV H$^+$ ions in TiO$_2$. The red curve is derived from the Mermin energy loss function with Fuentes data [19,29]. The green short-dashed-dot is obtained with the Drude-Lorentz dielectric function with Fuentes [29] and the blue dashed line corresponds to this work.

to the first derivative of V_{ind} at $\rho = 0$ and $\tilde{z} = 0$). Indeed, the electronic stopping powers are 11.9 eV/Å and 12.0 eV/Å for Mermin and Drude-Lorentz respectively using Fuentes data, and 15.7 eV/Å for Drude-Lorentz using the present data. Moreover, all of them produce about the same values for the Coulomb broadening when one considers a H_2^+ beam (150 keV/u, normal incidence) into a 10 nm thick TiO_2 film, namely 530 eV and 529 eV for Mermin and Drude-Lorentz respectively using Fuentes data, and 529 eV for Drude-Lorentz using present data. In particular, the very similar results obtained for the Coulomb broadening is a direct consequence of the similarity of the wake potentials shown in Fig. 5. Despite the differences, the shape of the curves are nearly the same, leading to similar wake forces. In what follows, we make use of the Mermin-type dielectric function because of its improved built-in dispersion relation.

B. Neutralization

According to semiempirical formulas [36] for the mean charge state of protons traversing a solid, the neutralization of protons is expected to be important for energies smaller than 100 keV/u. From the experimental point of view, the neutralization of the fragments is observed by comparing the total yield of the MEIS spectrum for different energies. Since the neutral fraction of H^0 is not detected, as the MEIS setup uses an electrostatic analyzer, the corresponding reduction of the total yield of the Ti peak (normalized by the scattering cross section) is consistent with the increasing of H^0 charge-state fraction [36,37].

In the Monte Carlo simulations we assume that the neutralization of H^+ ions takes place inside the solid according to the electron capture and loss cross sections as discussed in Ref. [6]. An estimate of the electron loss cross section for H^0 particles in TiO_2 as a function of energy was obtained from experimental results for CO_2 gas targets [38]. The capture cross section is then calculated based on the constraint that it should reproduce the value of the mean charge state from Ref. [36]. The uncertainty in the determination of the electron loss cross section affects only the mean distance for charge-exchange processes and has a minor effect on the simulated values of the Coulomb broadening.

The mean charge state of each moving fragment is affected by the presence of the nearby fragment. This vicinage effect on the charge state was observed in carbon foils [39] as a function of the H_2^+ ion energy and was used here to correct the values of the mean charge state from Ref. [36]. A multiplicative correction factor was used and amounts 0.91 at 30 keV/u and 0.94 at 120 keV/u [39] and interpolated/extrapolated values were used for the energies studied in this work.

Another effect that has to considered is the modification of the atomic radius of the H^0 fragment by the wake potential generated by its nucleus just after the capture process. In fact, the atomic radius of an embedded H^0 is larger than the Bohr radius a_0 (0.529 Å). This effect modifies the total force acting upon that neutral fragment due to a neighboring positive fragment. In order to take this effect into account, we describe the H^0 bound electron density $\rho(r)$ by an effective charge Z_{eff} according to $\rho(r) = A \exp(-2Z_{eff}r)$, where A is a normalization constant. Thus, the atomic radius will simply be a_0/Z_{eff}. The Z_{eff} is obtained from the variational principle

TABLE III. The values of Z_{eff} and bound state radius r_{bound} ($=1/Z_{eff}$) as a function of H^0 kinetic energy.

Energy (keV)	Z_{eff}	r_{bound}
30	0.74	1.35
50	0.79	1.27
70	0.83	1.20
100	0.87	1.15
150	0.90	1.11
200	0.93	1.08

taking into account not only the Coulomb interaction from the moving nucleus but also the wake potential generated by the same nucleus according to Eq. (3) (see Table III). No vicinage effect was taken into account for the determination of Z_{eff}.

C. Multiple scattering

The effect of the nuclear collisions are taken into account by the Monte Carlo simulations but turn out to be of minor importance since the TiO_2 films are not thick enough to produce a sizable effect. While multiple scattering events affect the distribution of internuclear distances at larger depths, it has a negligible effect at smaller depths according to the present simulations. Therefore, at the energies studied in this work, nuclear multiple scattering does not contribute significantly to σ_C.

IV. RESULTS AND DISCUSSIONS

The results for the Coulomb broadening σ_C for 50, 120, and 150 keV/u H_2^+ ions traversing the thin TiO_2 film as a function of the apparent thickness [thickness/$\cos(\theta)$, where θ is the incidence angle] are shown in Fig. 6. The Coulomb broadening values and the apparent thicknesses were obtained from the best fit of the MEIS energy spectra for three different scattering angles (112°, 120° and 128°). The uncertainties associated with the Coulomb broadening were estimated based on the χ^2 minimization procedure. The thicknesses are expressed in terms of atoms/cm^2. Moreover, it is important to stress that the experimental results for the Coulomb broadening σ_C (vertical axis) and the total amount of atoms (horizontal axis) do not depend on the film density used in the fitting analysis. The solid curves displayed in Fig. 2 correspond to the simulations described in Sec. III assuming a TiO_2 density of 3.4 g/cm^3 to convert the depth scale from nanometers to atoms/cm^2. In fact, this density is the one that provides the best fit of the 1D energy spectra such as those shown in Fig. 2. It is important to note that this density is 10% lower than the one of TiO_2 in the amorphous phase, i.e 3.8 g/cm^3 [40]). The use of 3.4 g/cm^3 in the simulations led to a thickness of 10 nm for the TiO_2 film. This thickness is in good agreement with transmission electron microscopy (TEM) images as the ones shown in Fig. 7. This image also shows the presence of voids in the TiO_2 film, which confirms a decrease in film density. Figure 6 also shows that the values of σ_C as well as its dependence on film thickness are larger for increasing projectile energies.

We have also performed ellipsometry measurements to determine the thickness of the TiO_2 film. Wavelengths ranging from 0.37–0.63 μm were used in these experiments. The results obtained for the film thickness was 10 ± 2 nm, while
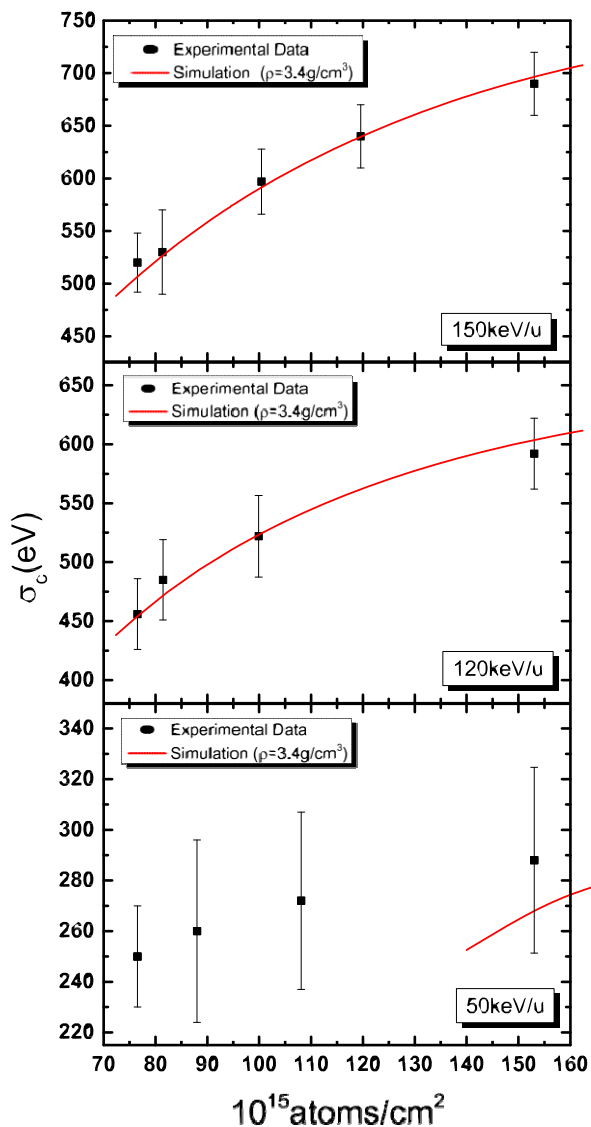
FIG. 6. (Color online) The Coulomb broadening as a function of the depth traversed by the fragments of H_2^+ molecules in ultrathin TiO_2 film obtained at energies of 50, 120, and 150 keV/u. The curves represent the calculations of the Coulomb broadening assuming a Coulomb repulsive potential screened by the wake potential.

FIG. 7. (a) High-resolution TEM image of the TiO_2 film using phase contrast. (b) Scanning transmission electron microscope (STEM) image of the same sample. In (b) no difference could be observed between the contributions of TiO_2 and SiO_2, present as a native oxide.

the refractive index varied from 2.58 at 0.37 μm to 2.21 at 0.63 μm. These values are slightly smaller than those from bulk TiO_2, which confirms the relatively lower density of the TiO_2 film.

The Coulomb depth profile technique yields the same film thickness for all energies only if wake and neutralization effects are properly taken into account. As expected, these effects decrease the energy loss straggling due to the Coulomb explosion at lower energies. The importance of each effect as a function of the energy for the H_2^+ molecules is depicted in Fig. 8. The Coulomb broadening σ_C, evaluated after 20 nm, traversed by two H^+ fragments and assuming a pure Coulomb repulsion potential, is shown as a black solid curve. It increases with the ion energy because it depends on the product of the ion velocities in the laboratory and CM systems after a complete Coulomb explosion. On the other hand, for a fixed
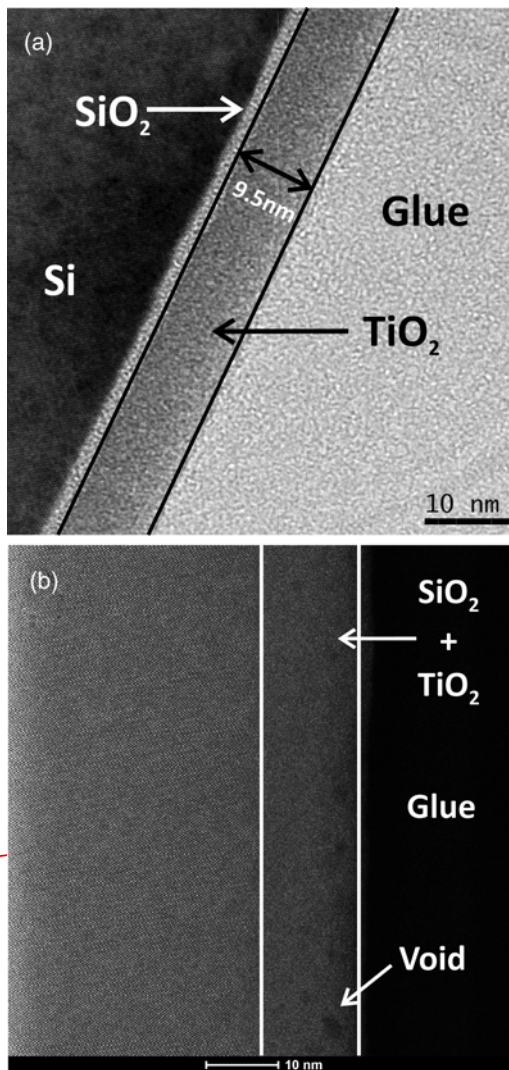
traversed distance, the dwell time decreases as the ion velocity increases, thus reducing the effect of the explosion but the simulation shows that this is less important. The screening effect from the Yukawa screening function (with screening length given by v/ω_p, with $\omega_p = 12.1$ eV [41]) reduces the effect of the Coulomb explosion mainly for low energies. The Coulomb explosion assisted by wake forces (dashed line in Fig. 8) yields σ_C values that are smaller at low energies and larger at higher energies when compared with the free Coulomb explosion (i.e., the Coulomb explosion expected for H^+-H^+ in vacuum). For lower energies, the wake potential has a screening effect similar to the Yukawa potential. At energies larger than 150 keV/u, the wake force on the trailing proton tends to align this fragment behind the leading proton [13]. This alignment increases the value of σ_C. In all cases, the neutralization, which plays an important role at energies lower than 100 keV/u, weakens the Coulomb explosion and thus decreases σ_C. At 150 keV/u, the simple free Coulomb
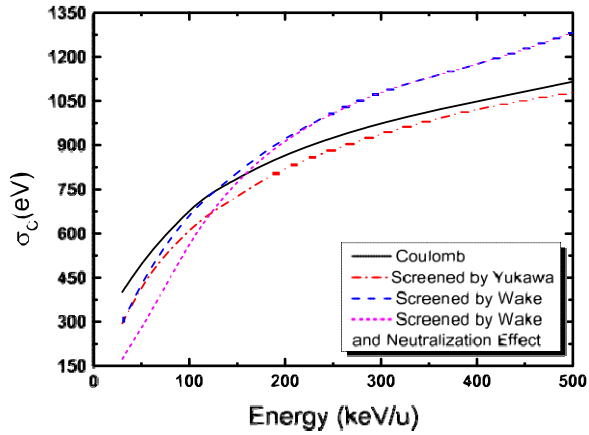
FIG. 8. (Color online) The Coulomb broadening (σ_C) as a function of the H_2^+ energy for ions traversing a 10 nm thick TiO_2 film along a trajectory 60 degrees away from the surface normal. The lines stand for calculations of σ_C in different scenarios: assuming a free Coulomb explosion (full black line); assuming the Coulomb repulsive potential screened by Yukawa potential (dot-dashed red line); assuming a Coulomb repulsive potential screened by wake potential (dashed blue line). All calculations were obtained assuming two H^+ fragments. The purple curve includes the possibility of having H^0 fragments.

FIG. 9. (Color online) On the right the Coulomb broadening σ_C for three fixed initial H_2^+ orientations ($\Theta_{in} = 0°, 30°$, and $80°$) at 200 keV/u. On the left the distribution of final cluster orientations after traversing a layer of 200 Å.

explosion model yields the same Coulomb broadening as the more sophisticated calculations for the present case.

Figure 9 shows the results of Monte Carlo simulations where the initial orientation Θ_{in} of the clusters is not randomized for a H_2^+ beam at 200 keV/u. On the left panels, σ_C is shown as a function of thickness for two interacting potentials and three initial orientations, namely $\Theta_{in} = 0°, 30°$, and $80°$ (see inset of Fig. 9). On the right panels, it is shown the corresponding distributions of angular orientations after a thickness of 200 Å is traversed by the ions. For the sake of clarity, multiple-scattering effects due to collisions with the target nuclei (Ti and O) have been turned off. Therefore, for a central potential as the Coulomb potential, the final angular orientations are identical to the initial orientations. On the other hand, a change in alignment is clearly observed for the wake interaction. For initial orientations corresponding to $\Theta_{in} = 30°$ and $80°$, a large fraction of the fragments are rotated towards smaller value of Θ, which will enhance σ_C. In fact, the wake potential has two effects: alignment and screening. The enhancement of σ_C due to the alignment is clearly visible for $\Theta_{in} = 80°$. For this case, screening is of minor importance since trailing H^+ ions are out of the wake. For $\Theta_{in} = 0°$, no alignment takes place and the wake potential just screens the Coulomb interaction, yielding a smaller value of σ_C. For $\Theta_{in} = 30°$, both effects compensate each other.

V. CONCLUSIONS

In this work we exploit the Coulomb explosion of H_2^+ molecules in order to improve the depth profiling capabilities
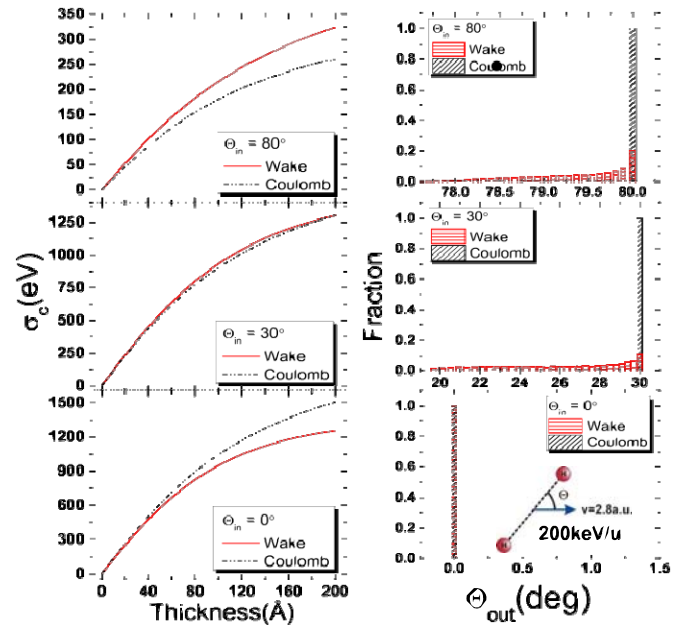
of ion scattering techniques at energies lower than 200 keV/u. The correct interpretation of the energy-loss straggling σ_C due to the Coulomb explosion allows the determination of the dwell time of the fragments before the backscattering collision. Consequently, the film thickness and the corresponding density can be obtained in a straightforward manner. At low energies, neutralization and wake effects are shown to be important and their influence on σ_C can be accurately modeled by Monte Carlo simulations. The neutralization is also affected by the presence of the wake potential and vicinage effects. At high energies, only the wake forces acting upon the charged fragments are important and can enhance the value of σ_C compared to a free Coulomb explosion. For the TiO_2 film studied in this work we obtained the same thickness at different projectile energies indicating that the energy dependences of the different contributions are modeled correctly. The validity of the present results were checked by TEM and STEM measurements. The lower density found in our targets is explained by the presence of voids as observed by STEM.

[1] S. M. Shubeita, R. C. Fadanelli, J. F. Dias, and P. L. Grande, Surf. Sci. **608**, 292 (2013).

[2] M. J. Gaillard, J.-C. Poizat, A. Ratkowski, and J. Remillieux, Nucl. Instrum. Methods **132**, 69 (1976).

[3] R. Levi-Setti, K. Lam, and T. Fox, Nucl. Instrum. Methods **194**, 281 (1982).

[4] A. L'Hoir, C. Cohen, J. J. Ganem, I. Trimaille, I. C. Vickridge, and S. M. Shubeita, Phys. Rev. A **85**, 042901 (2012).

[5] M. Gaillard, J.-C. Poizat, J. Remillieux, A. Chateau-Thierry, A. Gladieux, and W. Brandt, Nucl. Instrum. Methods **132**, 547 (1976).

[6] M. C. Cross, Phys. Rev. B **15**, 602 (1977).

[7] C. D. Denton, I. Abril, M. D. Barriga-Carrasco, R. Garcia-Molina, G. H. Lantschner, J. C. Eckardt, and N. R. Arista, Nucl. Instrum. Methods Phys. Res., Sect. B **193**, 198 (2002).

[8] P. de Vera, I. Abril, and R. Garcia-Molina, Appl. Radiat. Isot. **83, Part B**, 122 (2014).

[9] I. Abril, J. C. Moreno-Marín, J. M. Fernandez-Varea, C. D. Denton, S. Heredia-Avalos, and R. Garcia-Molina, Nucl. Instrum. Methods Phys. Res., Sect. B **256**, 172 (2007).

[10] P. de Vera, R. Garcia-Molina, I. Abril, and A. V. Solov'yov, Phys. Rev. Lett. **110**, 148104 (2013).

[11] S. Heredia-Avalos, R. Garcia-Molina, J. M. Fernández-Varea, and I. Abril, Phys. Rev. A **72**, 052902 (2005).

[12] R. Garcia-Molina, C. D. Denton, I. Abril, and N. R. Arista, Phys. Rev. A **62**, 012901 (2000).

[13] C. D. Denton, I. Abril, R. Garcia-Molina, and S. Heredia-Avalos, Nucl. Instrum. Methods Phys. Res., Sect. B **256**, 137 (2007).

[14] J. F. V. der Veen, Surf. Sci. Rep. **5**, 199 (1985).

[15] J. R. Tesmer and M. A. Nastasi, *Handbook of Modern Ion Beam Materials Analysis: Materials Research Society*, 1st ed. (MRS, Pittsburgh, 1995).

[16] M. A. Sortica, P. L. Grande, G. Machado, and L. Miotti, J. Appl. Phys. **106**, 114320 (2009).

[17] W. K. Chu, *Backscattering Spectrometry* (Academic Press, New York, 1978).

[18] J. F. Ziegler, M. D. Ziegler, and J. P. Biersack Nucl. Instrum. Methods Phys. Res., Sect. B **268**, 1818 (2010).

[19] S. Limandri, R. Fadanelli, M. Behar, L. Nagamine, J. Fernández-Varea, I. Abril, R. Garcia-Molina, C. Montanari, J. Aguiar, D. Mitnik, J. Miraglia, and N. Arista, Eur. Phys. J. D **68**, 194 (2014).

[20] W. K. Chu, Phys. Rev. A **13**, 2057 (1976).

[21] S. M. Shubeita, M. A. Sortica, P. L. Grande, J. F. Dias, and N. R. Arista, Phys. Rev. B **77**, 115327 (2008).

[22] P. L. Grande, A. Hentz, R. P. Pezzi, I. J. R. Baumvol, and G. Schiwietz, Nucl. Instrum. Methods Phys. Res., Sect. B **256**, 92 (2007).

[23] E. P. Kanter, P. J. Cooney, D. S. Gemmell, K. O. Groeneveld, W. J. Pietsch, A. J. Ratkowski, Z. Vager, and B. J. Zabransky, Phys. Rev. A **20**, 834 (1979).

[24] G. Molière, Z. Naturforsch. A **2**, 133 (1947).

[25] I. Abril, R. Garcia-Molina, C. D. Denton, F. J. Pérez-Pérez, and N. R. Arista, Phys. Rev. A **58**, 357 (1998).

[26] M. D. Barriga-Carrasco and C. Deutsch, Plasma Phys. Controlled Fusion **48**, 1787 (2006).

[27] M. Behar, R. C. Fadanelli, I. Abril, R. Garcia-Molina, C. D. Denton, L. C. C. M. Nagamine, and N. R. Arista, Phys. Rev. A **80**, 062901 (2009).

[28] N. Mermin, Phys. Rev. B **1**, 2362 (1970).

[29] G. G. Fuentes, E. Elizalde, F. Yubero, and J. M. Sanz, Surf. Interface Anal. **33**, 230 (2002).

[30] I. Abril (personal communication).

[31] F. Yubero and S. Tougaard, Surf. Interface Anal. **19**, 269 (1992).

[32] M. Vos and P. L. Grande [Nucl. Instrum. Methods Phys. Res., Sect. B (to be published)], doi: 10.1016/j.nimb.2014.11.083.

[33] S. Tougaard and I. Chorkendorff, Phys. Rev. B **35**, 6570 (1987).

[34] U. Fano, Annu. Rev. Nucl. Sci. **13**, 1 (1963).

[35] C. T. Chantler and J. D. Bourke, Phys. Rev. B **90**, 174306 (2014).

[36] G. Schiwietz and P. L. Grande, Nucl. Instrum. Methods Phys. Res., Sect. B **175–177**, 125 (2001).

[37] G. Schiwietz and P. L. Grande, Nucl. Instrum. Methods Phys. Res., Sect. B **153**, 1 (1999).

[38] Y. Nakai, T. Shirai, T. Tabata, and R. Ito, At. Data Nucl. Data Tables **37**, 69 (1987).

[39] B. Mazuy, A. Belkacem, M. Chevallier, M. J. Gaillard, J.-C. Poizat, and J. Remillieux, Nucl. Instrum. Methods Phys. Res., Sect. B **33**, 105 (1988).

[40] D. Mergel, D. Buschendorf, S. Eggert, R. Grammes, and B. Samset, Thin Solid Films **371**, 218 (2000).

[41] D. W. Fischer, Phys. Rev. B **5**, 4219 (1972).